Rapid Modeling of Photopolymerization in Projection Two-Photon Lithography Via an Operator Splitting Finite Difference Method

Rushil Pingali[1]
George W. Woodruff School of Mechanical Engineering
Georgia Institute of Technology
Atlanta, GA 30332, USA

Sourabh K. Saha[2]
George W. Woodruff School of Mechanical Engineering
Georgia Institute of Technology
Atlanta, GA 30332, USA
e-mail: ssaha8@gatech.edu
ASME Member

Abstract

Two-photon lithography (TPL) is an attractive technique for nanoscale additive manufacturing of functional 3D structures due to its ability to print sub-diffraction features with light. Despite its advantages, it has not been widely adopted due to its slow point-by-point writing mechanism. Projection TPL (P-TPL) is a high-throughput variant that overcomes this limitation by enabling the printing of entire 2D layers at once. However, printing the desired 3D structures is challenging due to the lack of fast and accurate process models. Here, we present a fast and accurate physics-based model of P-TPL to predict the printed geometry and the degree of curing. Our model implements a finite difference method enabled by operator splitting to solve the reaction-diffusion rate equations that govern photopolymerization. When compared with finite element simulations, our model is at least a hundred times faster and its predictions lie within 5% of the predictions of the finite element simulations. This rapid modeling capability enabled performing high-fidelity simulations of printing of arbitrarily complex 3D structures for the first time. We demonstrate how these 3D simulations can predict those aspects of the 3D printing behavior that cannot be captured by simulating the printing of individual 2D layers. Thus, our models provide a resource-efficient and knowledge-based predictive capability that can significantly reduce the need for guesswork-based iterations during process planning and optimization.

Keywords: multi-photon polymerization, additive manufacturing, nanomanufacturing, direct laser writing, physics-based simulations

---

[1] Current address: Department of Materials Science and Engineering, Northwestern University, email: rushilpingali@u.northwestern.edu
[2] Corresponding author

1. Introduction

Two-photon lithography (TPL) is a photopolymerization-based technique that offers the ability to additively manufacture cm-scale three-dimensional (3D) structures with 100 nm-scale features [1-3]. TPL relies on non-linearities in the absorption of high-intensity light from a femtosecond laser and the subsequent polymerization chemistry to achieve resolutions that are smaller than the optical diffraction limit [1]. Thus, TPL has found applications in a diverse range of research areas, such as medicine [4, 5], microelectronics [6], mechanical metamaterials [7-9], optical metamaterials [10, 11], and micromachines [12, 13]. Although TPL is an attractive choice for prototyping, its deployment beyond the laboratory has been hindered by its low printing rate. A conventional TPL system scans a focused laser spot point-by-point, creating and overlapping individual polymerized volumes (i.e., "voxels") to build up a 3D structure. The slow processing is a consequence of the low scanning speed that lies between 10 μm s^{-1} and 100 mm s^{-1} [14]. Several approaches have been demonstrated recently that increase the throughput of TPL via parallelization, rapid serial scanning, or a combination of the two techniques [15-18]. However, these approaches have not yet been well-studied and predictive process models for these approaches are lacking. Consequently, printing of the desired 3D structures requires slow and error-prone guesswork-based iterations. Here, we focus on overcoming this challenge for the projection two-photon lithography (P-TPL) process, which is a high-throughput implementation of TPL. We present a physics-based model of photopolymerization to enable rapid and accurate predictions of the 3D printed geometry and the degree of curing during P-TPL.

P-TPL is a high-throughput technique that replaces the serial scanning scheme of conventional TPL with a layer-by-layer projection scheme. We have previously demonstrated that P-TPL can increase the throughput by up to three orders of magnitude with no loss of resolution [15]. A schematic of the P-TPL system is shown in Fig. 1. In this technique, a patterned 2D femtosecond light sheet is projected within the photopolymer material to cure a thin layer of the material around the focal plane. A key element of P-TPL is that the light sheet is focused in both the space and the time domains by temporally stretching and re-compressing the femtosecond pulses [15]. This ensures that a strong axial gradient of light dosage exists around the focal plane, thereby achieving axial (i.e., depth) resolutions on the scale of 1 μm. A digital mask is applied using a digital micromirror device (DMD) to pattern the beam. The DMD consists of more than a million micromirrors and each one of them can be independently switched on or off to act as a switchable pixel (px). Femtosecond laser light, that is reflected from the DMD, initiates polymerization in those regions of photopolymer that correspond to the illuminated pixels of the DMD. Therefore, the entire X-Y plane can be printed at once and the rate of printing is independent of the density or complexity of the projected pattern. An X-Y-Z stage allows for repositioning of the photopolymer relative to the focal plane for printing at different planes. 3D structures are generated by updating the image on the DMD and printing at the different X-Y planes.

Models that can accurately predict the printing outcomes are highly valuable for process planning, control, and optimization. However, physics-based models of TPL are not readily available as only a few studies have modeled the photopolymerization mechanisms underlying TPL [19-24]. We suspect that it is because of the significant challenges involved in computationally modeling photopolymerization at the time scales of TPL. During conventional TPL, the relevant physical processes vary over time scales ranging from tens of ns to minutes, i.e., on a time scale spanning at least ten orders of magnitude [25]. It is computationally challenging to perform physics-based simulations over such a long period. We have previously demonstrated that accurate 2D finite element (FE) models of photopolymerization in P-TPL can be developed by taking advantage of its area projection scheme, which significantly reduces the time complexity [23]. However, 3D models have remained elusive due to the computational complexity of the problem. Here, we overcome this challenge by presenting a finite difference method (FDM) that implements operator splitting to achieve rapid and accurate modeling of 3D printing in P-TPL.

Our choice of the simulation technique was driven by the need to overcome the speed versus accuracy tradeoff that exists in computational modeling of manufacturing processes. In general, FE models are highly accurate, but they are very slow for 3D simulations [26]. In contrast, data-driven machine learning (ML) models can rapidly predict the process outcomes, but they are not as accurate as FE models [27]. For P-TPL, we have demonstrated how neural network (NN)-based surrogate ML models can rapidly predict whether printing would occur under a given set of conditions to >98% accuracy [28]. However, these models could not accurately predict the size of the printed structures because of their poor fidelity. There are many manufacturing problems that demand both speed and accuracy of predictions simultaneously. For example, predicting the dimensions of the 3D printed structures with varying cross-sections requires accurate 3D modeling of the reaction-diffusion equations in P-TPL. This is beyond the capabilities of the NN surrogate models, and it would take an FE simulation on the order of days to perform a single simulation. Fast and accurate predictions are also necessary to solve the inverse design problem, whereby the processing parameters required for a desired printing outcome are determined through computation. Optimization of this nature would require many forward design simulations, which would be impractically slow using FE simulations. Thus, it is desirable to develop a P-TPL model that is capable of fast and accurate predictions.

Here, we demonstrate how an operator splitting approach combined with a finite difference method (FDM) can provide deterministic, physics-based, highly accurate 2D and 3D models of photopolymerization in P-TPL. Both FDM and FE method simulate physical phenomena by discretizing and solving the physics-based partial differential equations that describe the phenomena [29]. However, FDM solves partial differential equations via finite difference approximations that are often performed on uniform grids. In contrast, the FE method solves partial differential equations via variational techniques over mesh elements which are better suited for discretizing complex geometries [30, 31]. For simple geometries that can be readily discretized into uniform grids, this distinction often leads to FDM being faster and easier to implement than FE methods due to the ease of computing with uniform grids [29, 30]. This makes FDM particularly well suited for simulating photopolymerization in P-TPL because the simulations are performed over a cuboid geometry, which is simple enough to be discretized using a uniform 3D grid. However, for problems that have multiple coupled physical phenomena, such as the reaction-diffusion problem, FDM can become slow and inaccurate [32, 33]. This challenge in FDM has been overcome in the past by applying operator splitting techniques wherein the terms of the equations that arise from the different physics are computed separately at each time step [33, 34]. For example, operator splitting has been applied for the modeling of reaction-diffusion equations in combustion problems and in the modeling of epidemics [35, 36]. However, these techniques have not yet been applied for the modeling of photopolymerization during TPL. Here, we: (i) present a formulation of the operating splitting FDM (OS-FDM) to model the reaction-diffusion equations of P-TPL photopolymerization and (ii) demonstrate that the predictions are both fast and accurate.

2. Modeling Methods

2.1. Reaction-Diffusion Model of Photopolymerization

The photopolymerization process in TPL is governed by the coupled physical phenomena of chemical reactions and diffusion of chemical species [19]. Upon absorption of light by the photopolymer material, radicals (i.e., reactive species) are generated locally in it. For acrylate-based photopolymers, such as those used in P-TPL, these radicals initiate chain reactions in the photopolymer. These chain reactions lead to crosslinking via the formation of new covalent bonds between the carbon atoms of different photopolymer molecules. As the cross-linking process regenerates the radicals, the chain reactions can continue to crosslink (i.e., cure) the photopolymer until the radicals are terminated by reactions with those species that do not regenerate radicals. For example, radicals can be terminated by the dissolved oxygen that is present in the photopolymer [19]. Printing occurs when the degree of polymer curing (*DOC*) exceeds a threshold value (DOC_{th}) above which the material becomes insoluble in a solvent. Thus, the printing process is determined by the combination of the kinetics of the chemical reactions and the spatiotemporal evolution of the concentration of the chemical species via diffusion. The reaction and the diffusion phenomena are coupled because the species that react may also diffuse. Thus, coupled reaction-diffusion equations govern the photopolymerization process.

Previously, we have demonstrated that the following set of coupled partial differential equations (PDEs) constitutes an accurate model of the P-TPL polymerization process [23]:

$$\frac{\mathrm{d}}{\mathrm{d}t}[\mathrm{R}^*] = -k_p[\mathrm{P}][\mathrm{R}^*] - k_q[\mathrm{O}_2][\mathrm{R}^*] \tag{1}$$

$$\frac{\mathrm{d}}{\mathrm{d}t}[\mathrm{P}] = -k_p[\mathrm{P}][\mathrm{R}^*] - k_p[\mathrm{P}][\mathrm{P}^*] \tag{2}$$

$$\frac{\mathrm{d}}{\mathrm{d}t}[\mathrm{P}^*] = k_p[\mathrm{P}][\mathrm{R}^*] - k_t[\mathrm{O}_2][\mathrm{P}^*] \tag{3}$$

$$\frac{\mathrm{d}}{\mathrm{d}t}[\mathrm{O}_2] = -k_q[\mathrm{O}_2][\mathrm{R}^*] - k_t[\mathrm{O}_2][\mathrm{P}^*] + D_{O2}\left(\frac{\partial^2[\mathrm{O}_2]}{\partial x^2} + \frac{\partial^2[\mathrm{O}_2]}{\partial y^2} + \frac{\partial^2[\mathrm{O}_2]}{\partial z^2}\right) \tag{4}$$

$$\frac{\mathrm{d}}{\mathrm{d}t}[\mathrm{R}^\mathrm{x}] = k_q[\mathrm{O}_2][\mathrm{R}^*] \tag{5}$$

$$\frac{\mathrm{d}}{\mathrm{d}t}[\mathrm{P}^\mathrm{x}] = k_t[\mathrm{O}_2][\mathrm{P}^*] \tag{6}$$

In these equations, the square bracket notation [species] signifies the concentration of the chemical species. The species P represents the monomer (or oligomer) that undergoes cross-linking. The species R^* represents the primary radicals that are formed from the photoinitiator molecules upon illumination. The species P^* represents the secondary radicals that are formed during the cross-linking reactions when the primary radicals react with the species P. R^x represents the deactivated species formed when the primary radicals R^* react with oxygen (O_2), whereas P^x represents the deactivated species formed when the secondary radicals P^* react with oxygen. The deactivated species do not participate in the cross-linking process. The terms k_p k_q, and k_t represent the reaction rate constants for the polymerization (i.e., cross-linking) reactions, the quenching reactions between the primary radicals and oxygen, and the termination reactions between the secondary radicals and oxygen, respectively.

The optical input to the polymerizing system is provided through the output of the optical dosage model that predicts the distribution of optical dosage per pulse (D_p) in the focal volume. The term D_p is evaluated as the time integral of the square of the instantaneous intensity over the duration of the entire femtosecond pulse, and it represents the energy input per pulse during two-photon absorption. The optical dosage and intensity models that were used in this work are described elsewhere [15, 37]. After each femtosecond pulse, new primary radicals are generated in proportion to the dosage (D_p), the concentration of the photoinitiator (PI), the two-photon cross section of the PI molecule ($\sigma^{(2)}$), and the quantum efficiency of the PI molecule (Φ), which represents the efficiency of radical generation. This relationship is represented by

Eq. (7). The parameter h is the Planck's constant and v is the central frequency of the illumination beam. The set of Eqs. (1)-(7) represent the governing equations that govern photopolymerization in P-TPL. The parameters that were used here to solve these equations are listed in Table 1. These parameters were obtained from literature and our past work [19, 37, 38].

$$\Delta[\mathrm{R}^*] = \frac{D_p \sigma^{(2)} \Phi}{h^2 v^2}[\mathrm{PI}] \tag{7}$$

Here, Eq. (4) is the only equation with spatial derivative terms and these terms correspond to the diffusion of oxygen through the photopolymer. As oxygen is the smallest molecule amongst the reacting species, its diffusive effect on the kinetics of the reactions is strongest. The diffusion of molecules larger than oxygen has not been considered here because the diffusivity of such molecules is at least 10 times lower than that of oxygen. In previous versions of our model, we had accounted for the diffusion of R^*, which is the next larger species [23, 37]. However, we found that the diffusive effect of R^* is negligible because of the low diffusivity of R^* and because R^* is rapidly consumed before any appreciable diffusion can occur [37]. For other larger species, it has been demonstrated that their diffusive effects become dominant only at longer time scales on the order of a second [20], which is at least 100 times longer than the time scales of P-TPL exposures. Therefore, for all species other than oxygen, their concentrations at any spatial location and any point in time can be fully determined if the past concentrations of various species at that same point in space are known. That is, the concentrations of these species are not influenced by how their concentrations are changing at neighboring points. For these ordinary differential equations (ODEs), tracking any type of spatial gradients is unnecessary as the rate equations can be solved independently at each spatial location. Thus, we observe that if the ODEs were to be decoupled from the spatial derivative terms in Eq. (4) by decoupling the effect of oxygen, the memory and compute time requirements for modeling would be significantly reduced.

Nonetheless, oxygen diffusion is an important phenomenon in photopolymerization, and it cannot be abstracted away. An accurate model of oxygen diffusion is key to predicting chemical proximity effects, which is the primary advantage of this model over a simple optical model [37]. When we previously solved the reaction-diffusion model using the COMSOL software package, the FE method was applied to all variables and equations, which was computationally wasteful [23]. Here, we have overcome this challenge by applying an operator splitting method to Eq. (4). Operator splitting refers to obtaining a solution by separating the relevant governing differential equations into two or more parts, solving the parts separately at each time step, and then combining the solutions [34]. The terms of the equations are often separated by splitting the terms that represent the various physical phenomena [34]. Operator splitting also enables applying different numerical techniques to solve the split terms by optimizing the solver for each set of terms separately. Here, we have split Eq. (4) into two parts; one part represents the reaction phenomenon whereas the other part represents the diffusion phenomenon.

2.2. Operator splitting finite difference method (OS-FDM)

We have implemented the OS-FDM model of Eqs. (1) – (7) in the MATLAB software package. The flowchart of the code is illustrated in the appendix. The model parameters and the initial conditions for these simulations are the same as those used in our past FE simulation of P-TPL [37]. The model parameters are listed in Table 1 and the initial conditions are listed in Table 2. The OS-FDM simulation was performed on a uniform rectangular 2D grid (for 2D problems) and a uniform rectangular 3D grid (for 3D problems). The total number of nodes (N) can be obtained in terms of the nodes along the X, Y, Z axes as: $N=n_x \times n_y \times n_z$. To achieve faster simulations, computations were performed using N-length vectors wherever possible instead of 2D or 3D matrices. Each vector uses natural ordering, which for a finite difference discretization refers to numbering the nodes from left to right, bottom to top, and first page to last page [39]. Concentration vectors for each chemical species were created and set to their initial values that are listed in Table 2.

Here, we have performed computations with a uniform time step of 10 μs. As the period between the pulses is 200 μs, this value of time step is fine enough to capture the effect of individual femtosecond pulses on the polymerization process. At the beginning of the simulation, a list of those time steps was created at which pulse illumination events occur. As the duration of each pulse is at least 10^{-8} times shorter than the time step, each pulse event can be uniquely associated with a single time step. At these time steps, the effect of each femtosecond pulse illumination event was captured by updating the concentration of the primary radicals R^* and the PI using Eq. (7). To implement Eq. (7), a vector of the optical dosage at each node was created from the optical simulation. The concentration of R^* was increased by the value calculated from Eq. (7) and the concentration of PI was reduced by half that amount because each PI generates two primary radicals. This pulse tracking scheme is equivalent to making the approximation that each illumination event occurs instantaneously and that a significant unilluminated dark time exists until the next illumination event. This approximation is justified here due to the time scales of pulse duration and laser repetition rate, and it has been found to be accurate in our past FE simulations of P-TPL [23, 37].

At each time step, the concentrations of all chemical species other than O_2 were updated by solving Eqs. (1) – (3) and (5) – (6) using the fourth order Runge-Kutta (RK4) method [40]. The RK4 method was chosen because these equations form a set of coupled nonlinear ODEs. The RK4 method is explicit, so it does not require the solution of a nonlinear matrix equation, which is computationally expensive. At the same time, it is a higher order method and enables relatively larger time steps without an unacceptable increase in the accumulated error. To maximize computation speed, calculations were largely performed to single precision and the values of intermediate variables were memorized and reused wherever it was possible. It is noteworthy that for these computations, it is not necessary to know the concentration of O_2 at the current time step; instead, knowledge of the values from the previous time step is adequate. This allows one to solve Eqs. (1) – (3) and (5) – (6) separately from Eq. (4) at each time step, thereby representing the operator splitting aspect of this method. Nevertheless, these equations are still coupled with Eq. (4) because the effect of change in $[O_2]$ is captured in the next time step.

The concentration of O_2 was calculated at each time step by solving Eq. (4) with the updated values of $[R^*]$ and $[P^*]$, thus coupling Eq. (4) with the rest of the equations and linearizing the reaction terms. Computing the solution of Eq. (4) requires discretizing the spatial derivative term. This was done by using a centered difference approximation for the spatial derivative terms [39]. In two dimensions, based on a five-point stencil, Eq. (4) can be discretized over space as:

$$[O_2]'_{i,j} = -k_q[O_2]\left[\mathrm{R}^*\right]_{i,j} - k_t[O_2]\left[\mathrm{P}^*\right]_{i,j} + D_{O2}\left(\frac{[O_2]_{i-1,j}+[O_2]_{i+1,j}+[O_2]_{i,j-1}+[O_2]_{i,j+1}-[O_2]_{i,j}}{l^2}\right) \tag{8}$$

Here, *l* is the mesh node spacing and the LHS represents the time derivative of the concentration of O_2 at the spatial node (i, j). The formulation in three dimensions is identical except for the addition of terms representing adjacent nodes in the third dimension, i.e., the spatial derivatives were based on a seven-point stencil for a 3D problem. The implicit (backward) Euler method was used to solve Eq. (4) at each time step. This allows for the change in oxygen to be simulated without the loss of numerical stability. The standard formulation of the implicit Euler method is [41]:

$$y_{i+1} = y_i + \frac{dy_{i+1}}{dt}\Delta t \tag{9}$$

In order to represent this as a matrix operation, a sparse N × N matrix *A* was created to represent the dependency of the rate of change of $[O_2]$ at a given node on the values of $[O_2]$ at adjacent nodes; this is equivalent to using Eq. (8) to approximate the time derivative. When $[O_2]$ is a vector of the values of oxygen concentration at each of the N nodes listed in natural ordering, in two dimensions, Eq. (9) can be written as the matrix operation:

$$[O_2]_{current} = A \times [O_2]_{next} \tag{10}$$

where:

$$A = \begin{pmatrix} a_1 & a_2 & \cdots & a_2 & \cdots & & & & \\ a_2 & a_1 & a_2 & \cdots & a_2 & \cdots & & & \\ & & \ddots & & & & & & \\ a_2 & \cdots & a_2 & a_1 & a_2 & \cdots & a_2 & \cdots & \\ & & & & \ddots & & & & \\ \cdots & a_2 & \cdots & a_2 & a_1 & a_2 & \cdots & a_2 & \cdots \\ & & & & & & \ddots & & \\ & & & & \cdots & a_2 & \cdots & a_2 & a_1 \end{pmatrix} \tag{11}$$

$$a_1 = 1 + \Delta t\left(k_q[\mathrm{R}^*]_{i,j} + k_t[\mathrm{P}^*]_{i,j} + \frac{4D_{O2}}{l^2}\right) \tag{12}$$

$$a_2 = \left(\frac{-\Delta t D_{O2}}{l^2}\right) \tag{13}$$

In three dimensions, the formulation of Eq. (10) is similar, except that *A* has two additional off-diagonals of a_2 representing the additional connectivity in the third dimension. Solving Eq. (10) is the only step in this technique that requires direct matrix operations. Since *A* is symmetric positive definite (as it is Hermitian and strictly diagonally dominant), it can be solved very rapidly using the conjugate gradient method—indeed, more rapidly than it would take to iterate using a higher order explicit method.

Dirichlet boundary conditions were applied to represent the presence of abundant oxygen in the photopolymer beyond the region of printing by holding the oxygen concentration constant at its initial value at the boundary nodes. This allows for the simulation of only the area of interest while still capturing the effect of diffusion throughout the simulated volume. Dirichlet boundary conditions can be applied by replacing the rows and columns of A corresponding to boundary elements with identity matrices to keep them unchanging at their prescribed value. However, this approach causes A to become asymmetric and non-Hermitian. To preserve its good convergence properties, the boundary conditions are instead reapplied at each time step by changing the values of $[O_2]$ at boundary nodes to their prescribed values after solving Eq. (10).

By separately solving Eq. (4) and the set of Eqs. (1) – (3) and (5) – (6), the evolution of the concentrations of all species were computed over time. At each time step, the *DOC* was evaluated from the change in concentration of the species P as: *DOC* = (1- $[P]/[P]_o$). The subscript (o) notation indicates the initial value of the parameter. The value of the polymerization rate constant (k_p) was updated intermittently to account for the deceleration of the polymerization reaction with an increase in the *DOC*. The relationship between the k_p and the *DOC* was obtained from literature values [19]. For the range of values of *DOC* observed in this study, k_p was obtained by decreasing it linearly by 6% of its initial value for every 1% increase in the DOC. The parameter k_p was updated only when the change in the Euclidean norm of *DOC* over a time step exceeded a tolerance value, which was set to 0.001 here. At each time step, the printed region can be determined from the *DOC* distribution by evaluating the regions in which the computed *DOC* exceeds the solubility threshold DOC_{th}. Thus, the model presented here can be used to simulate both the printed geometry and the degree of polymer curing resulting from a given set of processing conditions.

3. Results and Discussions

3.1. 2D modeling

We have characterized the performance of the OS-FDM model by simulating the printing of benchmark 3D structures that exhibit translational symmetry along one axis. Specifically, we have simulated the printing of a single layer of an array of five lines with the projected linewidth of 5 pixel (px), a period of 30 px, and a length of 150 px. For our simulated P-TPL system, each pixel is demagnified to 113 nm in the projected image. The time-averaged optical power of the beam was 139 nW/px at the entrance of the objective lens. The rest of the optical system parameters were identical to those in our previous work [37]. The bitmap image for this printing operation is shown in Fig. 2(a). The image was projected for a total of 20 laser pulses at a laser repetition rate of 5 kHz, which resulted in an exposure time of 4 ms. Due to the symmetry of the lines along the length axis, this simulation problem reduces into a 2D problem. During the simulation, the evolution of the concentration of the various species was tracked through the exposure period and for a subsequent dark period of 100 ms. The simulation was performed over a 2D region that had a width of 30 μm along the lateral direction (i.e., X axis) and 10 μm along the axial direction (i.e., Z axis). The model was spatially discretized with a node spacing of 100 nm and temporally discretized with a time step of 10 μs. The concentration of the species at the non-node locations was obtained by spline interpolation.

The optical dosage distribution, the printed geometry, and the 2D *DOC* profile at various instants of time are shown in Figs. 2(b) – (f). The printed geometry was obtained by identifying the regions where the *DOC* at the end of the 100 ms dark period exceeds the DOC_{th}. The processing conditions simulated here result in the printing of five distinct lines corresponding to the five projected lines. The printed linewidths vary from 500 – 514 nm and the heights vary from 697 – 707 nm. The variations in the linewidth exist because the lines on the periphery are narrower than the lines at the center. As illustrated in Fig. 2(b), the optical dosage along the periphery is lower than the dosage at the center. Thus, the variation in the printed linewidth is consistent with the variation in the optical dosage. This demonstrates that the OS-FDM photopolymerization model can faithfully capture the effect of variations in the optical dosage (i.e., the optical input to the OS-FDM model) on the printing outcome (i.e., the *DOC* profile and feature size).

The OS-FDM model also enables tracking the temporal evolution of the concentrations of the various chemical species, as shown in Fig. 3. Each individual pulse of light can be tracked by the peaks in the R^* concentration. As expected, the primary radicals R^* are immediately consumed and some of them are converted into the secondary radicals P^*. The concentration of P^* increases in discrete steps corresponding to each pulse of light. After the end of the exposure period, the concentration of P^* decreases exponentially with time due to the termination reactions between P^* and O_2. This exponential decay is consistent with the predictions of FE models [37]. In the early stages, the concentration of O_2 decreases over time due to its consumption by the primary and secondary radicals. In the later stages, the concentration of O_2 begins to slowly rise due to the diffusion of O_2 from the surrounding medium. This initial drop and recovery in the concentration of O_2 is also consistent with the predictions of FE models [37]. Thus, the OS-FDM model can accurately capture the temporal evolution of the concentration of the chemical species during photopolymerization in P-TPL.

We have further characterized the accuracy of the OS-FDM model by comparing its feature size predictions to the predictions of a FE model. The printing parameters for these tests were identical to those used for the study shown in Fig. 2(f). The FE model was set up using the commercially available COMSOL package, which can simulate coupled reaction-diffusion phenomena. Our FE modeling technique is described in detail elsewhere [37]. To benchmark the performance of the two methods, the simulations were performed on the same workstation computer, which had an Intel® i7-9700K processor and 64 GB of RAM. The comparisons between OS-FDM and FE models were performed by varying the model discretization parameters. For the OS-FDM studies, the time step was fixed at 10 μs, but the node spacing was varied between 100 nm and 200 nm. These values for the node spacing were identified by performing a mesh convergence study, as shown in Fig. 4. The size of the central line was found to converge at node spacings of 200 nm and lower. For the FE studies, the number of mesh elements, which is equivalent to the number of nodes, was held constant based on a separate set of mesh convergence studies. The time step for the FE studies was varied by tuning the solver tolerance parameter. As an adaptive time stepping algorithm was implemented in the COMSOL model to optimize the speed, the time step could not be directly controlled. Despite this lack of quantitative information, it is qualitatively known that lower tolerances lead to shorter time steps. Therefore, this qualitative relationship was used here to compare the studies.

The results of the comparison tests are summarized in Table 3. For these tests, the prediction of the converged FE model with the smallest tolerance (i.e., first row in Table 3) was considered to be the ground truth value. The mean width and height refer to the average value of the widths and heights over the five lines. The percentage error in the width was calculated as the ratio of the root mean square error in the widths of the five lines and the mean width of the ground truth model. The percentage error in the height was evaluated similarly. It can be observed from Table 3 that the predictions of the OS-FDM model with the finest mesh are within 5% of the benchmark FE model predictions. The OS-FDM simulations were at least 300 times faster than the benchmark FE model and at least 100 times faster than the FE model with a poorer tolerance (i.e., second row in Table 3). Thus, the OS-FDM model significantly improves the speed of the simulations with a modest decrease in the accuracy.

At this point, one may criticize that an equivalent tradeoff between speed and accuracy can be achieved by simply using coarser discretization in the FE models; therefore, there is no net computational advantage to using OS-FDM. However, the data summarized in Table 3 demonstrates that this criticism is not valid here. Although coarsening the FE model did increase the speed, the FE model was still 50 times slower than the OS-FDM model. At the same time, the accuracy of the coarse FE model was worse than that of the

OS-FDM models. Thus, the speed versus accuracy tradeoff in FE models is not conducive to performing rapid and accurate simulations of P-TPL. In contrast, OS-FDM models can rapidly simulate photopolymerization in P-TPL with high fidelity. Therefore, the OS-FDM models provide a significant computational advantage over FE models.

3.2. 3D modeling

The computational advantage of OS-FDM has enabled us to perform high-fidelity physics-based 3D simulations of photopolymerization in P-TPL for the first time. Due to the extremely slow computations during FE modeling, it was previously impractical to perform high-fidelity 3D simulations. For example, with a mesh coarser than the mesh of the 2D FE simulations and a tolerance of 10^{-4}, it took 85,020 seconds (i.e., a day) to solve a 3D FE simulation of a 3D log-pile structure with 5 layers. In comparison, our OS-FDM model was able to solve the identical problem in 84 seconds with a coarse mesh (i.e., 200 nm spacing) and 733 seconds with a fine mesh (i.e., 100 nm spacing). Thus, the OS-FDM technique demonstrates a speedup of up to two orders of magnitude even for 3D problems, and it provides access to higher precision computational ability if so desired.

The simulation of photopolymerization in 3D enables performing such studies of P-TPL that cannot be performed with 2D simulations of single layers alone. For example, 3D simulations can reveal whether the projection of subsequent layers causes any additional printing in the adjacent layers. To demonstrate this, we have performed a set of 3D simulations of a log-pile printing operation that consisted of projecting three distinct layers. In each layer, a array of five lines was projected wherein the period of the array was 10 px, and each line was 7 px wide and 50 px long. Lines in each layer were oriented at right angles to the lines in the previous layer and the layers were separated by 500 nm. Each layer was projected for 2 ms, i.e., for a total of 10 pulses. The optical power of the beam was held constant at 200 nW/px. A node spacing of 100 nm was used for the OS-FDM simulations, and the simulations were performed over a cube of side length 10 μm. All other model parameters were identical to the parameters in the 2D OS-FDM models. The *DOC* of the entire volume was recorded periodically after 10 ms of dark time following the completion of each projection. The results of these studies are summarized in Fig. 5. Only those regions where the *DOC* exceeded the DOC_{th} are shown in the figure.

It was observed that the projection of the first layer led to the printing of five distinct lines with finite gaps between the lines. Projection of the second layer on top of this layer created a porous 3D log-pile structure. However, projecting the third layer on top of this structure led to excess printing that filled in the pores between the lines. This excess printing occurs due to the presence of the background dosage. To verify this, we have tracked the concentration of the various species and the *DOC* at the center of the central line in the first layer (i.e., at X=Y=Z=0). This data is shown in Fig. 6. It is observed that non-zero R^* concentrations arise in this spot when the second and the third layers are projected, beginning at 12 ms and 24 ms, respectively. These R^* concentrations are significantly lower than the R^* concentrations due to the projection of the first layer because the second and third layers are not focused at this plane. However, the concentration of O_2 is also lower at these later instants of time than at the beginning, which suppresses the inhibiting effect of O_2 on the polymerization reactions at these later times. Consequently, the increase in *DOC* due to these off-focal projections cannot be neglected here. The OS-FDM technique enables us to perform rapid iterative 3D simulations to identify processing conditions that would eliminate these defects. For example, upon repeating the printing with a lower power of 139 nW/px, no excess printing was observed, as illustrated in Fig. 7. It is noteworthy here that a 2D simulation of a single layer would have predicted the formation of distinct lines in both cases (i.e., higher and lower power), but the full multi-layer

3D simulation revealed differences between the two cases. Thus, OS-FDM enables performing such physics-based simulation studies of P-TPL that were not possible in the past.

As our OS-FDM simulations are performed on a cuboid volume using a uniform grid, the model performance is expected to be invariant to the geometric complexity of the printed structure provided the overall size of the simulated volume and the discretization parameters remain the same. We have verified this expectation by simulating the printing of an arbitrarily complex 3D structure (i.e., GT logo) comprising three different layers. The images projected in the three layers are shown in Figs. 8(a)-(c). Simulation was performed over the same volume (i.e., cube of side length 10 μm) and with the same discretization (i.e., node spacing of 100 nm) as used for simulating the 3D log-pile structure shown in Fig. 7. Each layer was projected for 2 ms, i.e., for a total of 10 pulses and the optical power of the beam was held constant at 139 nW/px. The layers were spaced along the depth direction at 700 nm. We observed no difference in the solve time for simulating the GT logo versus the 3D log-pile structure shown in Fig. 7 (difference < 0.2%). The resulting *DOC* profile is shown in Figs. 8(d) and (e). The three layers of the GT can be distinctly identified by the overhanging sections that are present in the second and the third layers. It is noteworthy that the solve time of our OS-FDM technique is invariant to both the complexity of the projected 2D bitmap images and the spacing of the layers, but it increases with an increase in the number of layers and a decrease in the node spacing (as shown in Table 3). For some complex 3D geometries, such as those with large curvatures or steep angles, one may want to tune both the number of layers and the node spacing to achieve accurate predictions, which will lead to longer simulations. Nevertheless, the OS-FDM simulations are significantly faster than the FE simulations and can therefore be applied to computationally simulate the printing of a variety of complex 3D structures.

3.3. Limitations and potential extensions of the model

As a first step, here we have validated the accuracy of the OS-FDM model by benchmarking it against the FE models. The FE models were themselves validated against empirical data from physical experiments [23]. It was previously observed that the FE models could accurately predict the feature widths, but the predicted heights were lower at higher exposures [23]. We suspect that this discrepancy occurs primarily due to the enhanced light absorption via single-photon absorption because the single-photon absorptivity of the cured polymer is higher than the uncured material [42]. To account for this effect, Eq. 7 must be updated with additional single-photon absorption terms. As the rest of the equations remain unchanged, the OS-FDM model formulation will stay the same.

Although our model was formulated for the P-TPL process, we anticipate that our OS-FDM approach can also be applied to predict the outcome of other TPL implementations. Our technique is well suited for those TPL implementations that use low repetition rate femtosecond lasers (i.e., rates of ~1 kHz), such as the high-throughput implementation based on digital holography [17] . Our model of photopolymerization can be adapted to such studies with minimal changes due to the similar time scale of illumination and polymerization reactions. To adapt our OS-FDM model to the more prevalent TPL implementations that use high repetition rate lasers (i.e., rates of ~100 MHz), one must modify the polymerization rate equations to include the illumination term within the differential rate equations. Nevertheless, our work demonstrates that OS-FDM is an accurate and rapid technique for physics-based simulation of photopolymerization.

4. Conclusions

In summary, we have demonstrated that an operator splitting finite difference method (OS-FDM) can accurately and rapidly simulate the outcome of the reaction-diffusion photopolymerization processes in P-

TPL. We have modeled photopolymerization in P-TPL via OS-FDM by representing the underlying physical phenomena through a set of partial differential equations that are coupled through the reaction and the diffusion terms. Operator splitting was achieved by splitting the reaction and diffusion terms so that the reaction terms could be solved without evaluating any spatial derivatives, while still capturing the effect of diffusion on the reactions in subsequent time steps. When compared with finite element simulations, operator splitting led to a computational speedup by 100 – 300 times and an accuracy within 5%. This significant speedup enabled performing high-fidelity 3D simulations of multi-layered 3D structures for the first time. The 3D simulations revealed additional modes of defects that could not be predicted from the 2D simulations of the single layers alone. Thus, OS-FDM enables rapid and high-fidelity physics-based simulation of photopolymerization in P-TPL. By significantly reducing the need for guesswork-based iterations during process planning and optimization, our work will enable scalable nanomanufacturing of complex 3D structures for various applications in computing, energy, transportation, and human health.

Appendix

A flowchart of the OS-FDM implementation is shown in Fig. A1.

Acknowledgments

This work was supported by the National Science Foundation CAREER grant 2045147 and in part through research cyberinfrastructure resources and services provided by the Partnership for an Advanced Computing Environment (PACE) at the Georgia Institute of Technology.

Conflict of Interest

The co-authors are inventors on pending and/or issued patent applications on P-TPL for which the intellectual property rights are assigned to either Georgia Tech Research Corporation or the Lawrence Livermore National Security LLC.

Data Availability Statement

The data sets generated and supporting the findings of this article are obtainable from the corresponding author upon reasonable request.

Nomenclature

Chemical species

PI	photoinitiator
R^*	primary radical
P	monomer
O_2	oxygen
P^*	secondary radical formed from monomer P
R^x	quenched primary radical
P^x	dead polymer chain

Symbols

k_p	polymerization rate constant at a specific degree of polymer conversion
k_q	radical quenching rate constant
k_t	termination rate constant
D_{O2}	diffusivity of O_2
DOC	degree of polymer conversion
DOC_{th}	threshold degree of polymer conversion
D_p	optical dosage per pulse
$\sigma^{(2)}$	two-photon cross-section of photoinitiator
h	Planck's constant
Φ	quantum yield of photoinitiator
v	frequency of light

References

1. Baldacchini, T., *Three-dimensional microfabrication using two-photon polymerization: fundamentals, technology, and applications*. 2015: William Andrew.
2. Jonušauskas, L., S. Juodkazis, and M. Malinauskas, *Optical 3D printing: bridging the gaps in the mesoscale.* Journal of Optics, 2018. **20**(5): p. 053001.
3. Sun, H.-B. and S. Kawata, *Two-photon photopolymerization and 3D lithographic microfabrication*, in *NMR• 3D Analysis• Photopolymerization*. 2004, Springer. p. 169-273.
4. Narayan, R.J., et al., *Medical prototyping using two photon polymerization.* Materials Today, 2010. **13**(12): p. 42-48.
5. Selimis, A., V. Mironov, and M. Farsari, *Direct laser writing: Principles and materials for scaffold 3D printing.* Microelectronic Engineering, 2015. **132**: p. 83-89.
6. Wu, E.-S., et al. *Two-photon lithography for microelectronic application*. in *Optical/Laser Microlithography V*. 1992. SPIE.
7. Bauer, J., et al., *Approaching theoretical strength in glassy carbon nanolattices.* Nature materials, 2016. **15**(4): p. 438-443.
8. Meza, L.R., S. Das, and J.R. Greer, *Strong, lightweight, and recoverable three-dimensional ceramic nanolattices.* Science, 2014. **345**(6202): p. 1322-1326.
9. Bauer, J., et al., *Nanolattices: an emerging class of mechanical metamaterials.* Advanced Materials, 2017. **29**(40): p. 1701850.
10. Hossain, M.M. and M. Gu, *Fabrication methods of 3D periodic metallic nano/microstructures for photonics applications.* Laser & Photonics Reviews, 2014. **8**(2): p. 233-249.
11. Wang, H., et al., *Two-Photon Polymerization Lithography for Optics and Photonics: Fundamentals, Materials, Technologies, and Applications.* Advanced Functional Materials, 2023: p. 2214211.
12. Huang, T.Y., et al., *3D printed microtransporters: Compound micromachines for spatiotemporally controlled delivery of therapeutic agents.* Advanced Materials, 2015. **27**(42): p. 6644-6650.
13. Soreni-Harari, M., et al., *Multimaterial 3D Printing for Microrobotic Mechanisms.* Soft Robotics, 2020. **7**(1): p. 59-67.
14. Cao, C., et al., *Click chemistry assisted organic-inorganic hybrid photoresist for ultra-fast two-photon lithography.* Additive Manufacturing, 2022. **51**: p. 102658.
15. Saha, S.K., et al., *Scalable submicrometer additive manufacturing.* Science, 2019. **366**(6461): p. 105-109.
16. Somers, P., et al., *Rapid, continuous projection multi-photon 3D printing enabled by spatiotemporal focusing of femtosecond pulses.* Light: Science & Applications, 2021. **10**(1): p. 199.
17. Ouyang, W., et al., *Ultrafast 3D nanofabrication via digital holography.* Nature Communications, 2023. **14**(1): p. 1716.
18. Hahn, V., et al., *Rapid assembly of small materials building blocks (Voxels) into large functional 3D metamaterials.* Advanced Functional Materials, 2020: p. 1907795.
19. Mueller, J.B., et al., *Polymerization Kinetics in Three-Dimensional Direct Laser Writing.* Advanced Materials, 2014. **26**(38): p. 6566-6571.
20. Yang, L., et al., *On the schwarzschild effect in 3D two-photon laser lithography.* Advanced Optical Materials, 2019. **7**(22): p. 1901040.
21. Sun, M., et al., *Modeling of two-photon polymerization in the strong-pulse regime.* Additive Manufacturing, 2022. **60**: p. 103241.
22. Johnson, J.E., Y. Chen, and X. Xu, *Model for polymerization and self-deactivation in two-photon nanolithography.* Optics Express, 2022. **30**(15): p. 26824-26840.

23. Pingali, R. and S.K. Saha, *Reaction-Diffusion Modeling of Photopolymerization During Femtosecond Projection Two-Photon Lithography.* Journal of Manufacturing Science and Engineering, 2022. **144**(2).
24. Uppal, N. and P.S. Shiakolas, *Modeling of temperature-dependent diffusion and polymerization kinetics and their effects on two-photon polymerization dynamics.* Journal of Micro/Nanolithography, MEMS and MOEMS, 2008. **7**(4): p. 043002-043002.
25. Mueller, J.B., J. Fischer, and M. Wegener, *Reaction mechanisms and in situ process diagnostics*, in *Three-Dimensional Microfabrication Using Two-photon Polymerization*. 2016, Elsevier. p. 82-101.
26. Zimmerman, W.B.J., *Multiphysics modeling with finite element methods*. Vol. 18. 2006: World Scientific Publishing Company.
27. Kudela, J. and R. Matousek, *Recent advances and applications of surrogate models for finite element method computations: A review.* Soft Computing, 2022. **26**(24): p. 13709-13733.
28. Pingali, R. and S. Saha, *Printability Prediction in Projection Two-Photon Lithography via Machine Learning Based Surrogate Modeling of Photopolymerization*, in *Manufacturing Science and Engineering Conference 2023*. 2023, ASME: New Brunswick, New Jersey.
29. Li, Z., Z. Qiao, and T. Tang, *Numerical solution of differential equations: introduction to finite difference and finite element methods*. 2017: Cambridge University Press.
30. Thomas, J.W., *Numerical partial differential equations: finite difference methods*. Vol. 22. 1998: Springer Science & Business Media.
31. Jagota, V., A.P.S. Sethi, and K. Kumar, *Finite element method: an overview.* Walailak Journal of Science and Technology (WJST), 2013. **10**(1): p. 1-8.
32. Edelson, D. and N.L. Schryer, *Modeling chemically reacting flow systems—i. A comparison of finite difference and finite element methods for one-dimensional reactive diffusion.* Computers & Chemistry, 1978. **2**(2): p. 71-74.
33. Ramos, J.I., *A review of some numerical methods for reaction-diffusion equations.* Mathematics and computers in simulation, 1983. **25**(6): p. 538-548.
34. MacNamara, S. and G. Strang, *Operator Splitting*, in *Splitting Methods in Communication, Imaging, Science, and Engineering*, R. Glowinski, S.J. Osher, and W. Yin, Editors. 2016, Springer International Publishing: Cham. p. 95-114.
35. Wichman, I.S., *On the use of operator-splitting methods for the equations of combustion.* Combustion and flame, 1991. **83**(3-4): p. 240-252.
36. Ahmed, N., et al., *Positivity preserving operator splitting nonstandard finite difference methods for SEIR reaction diffusion model.* Open Mathematics, 2019. **17**(1): p. 313-330.
37. Kim, H., R. Pingali, and S.K. Saha, *Rapid printing of nanoporous 3D structures by overcoming the proximity effects in projection two-photon lithography.* Virtual and Physical Prototyping, 2023. **18**(1): p. e2230979.
38. Rumi, M., et al., *Structure−Property Relationships for Two-Photon Absorbing Chromophores: Bis-Donor Diphenylpolyene and Bis(styryl)benzene Derivatives.* Journal of the American Chemical Society, 2000. **122**(39): p. 9500-9510.
39. Greenbaum, A., *Iterative methods for solving linear systems*. 1997: SIAM.
40. Tan, D. and Z. Chen, *On a general formula of fourth order Runge-Kutta method.* Journal of Mathematical Science & Mathematics Education, 2012. **7**(2): p. 1-10.
41. Chapra, S.C. and R.P. Canale, *Numerical Methods for Engineers*. 2010: McGraw-Hill Higher Education.
42. Saha, S.K., et al., *Effect of proximity of features on the damage threshold during submicron additive manufacturing via two-photon polymerization.* Journal of Micro and Nano-Manufacturing, 2017. **5**(3).

Figure Captions List

Figure 1: Schematic of P-TPL. (a) Overview of the process and (b) overview of the system. (Reprinted with permission from Saha et al. [15]. Copyright by AAAS).

Figure 2: Results of 2D simulations performed with OS-FDM. (a) Bitmap image, (b) simulated optical dosage profile, (c) cross-sectional view of the simulated printed lines, i.e., regions where predicted $DOC > DOC_{th}$, (d) *DOC* profile at the end of the exposure ($t_e = 4$ ms). (e) *DOC* profile after 10 ms following the end of exposure, (f) *DOC* profile after 100 ms following the end of exposure. The same color bar applies to (d) – (f).

Figure 3: Temporal evolution of the concentration of various chemical species and the *DOC* at the center of the central line, obtained from the 2D OS-FDM simulation.

Figure 4: Mesh convergence of the 2D OS-FDM simulations.

Figure 5: *DOC* profile from 3D OS-FDM simulations of multi-layered log-pile printing. (a) 10 ms after projection of the first layer, (b) 10 ms after projection of the second layer, (c) 10 ms after projection of the third layer. The same color bar applies to all sub-parts. Optical power was 200 nW/px.

Figure 6: Temporal evolution of the concentration of various chemical species and the *DOC* at the center of the central line of the first layer, obtained from the 3D OS-FDM simulation.

Figure 7: *DOC* profile from 3D OS-FDM simulation of a multi-layered porous log-pile printed with an optical power of 139 nW/px. Profile was captured 10 ms after the projection of the third layer.

Figure 8: 3D OS-FDM simulation for printing of an arbitrarily complex 3D structure. (a)-(c) Digital images projected on three different layers, ordered from first layer (leftmost) to last layer (rightmost). (d) Simulated *DOC* profile of a three-layered structure printed with an optical power of 139 nW/px. (e) *DOC* profile of the same structure as viewed from a different orientation. 3D profiles were captured 10 ms after the projection of the third layer.

Figure A1: Flowchart for implementing OS-FDM for simulation of photopolymerization in P-TPL.

Figure 1:

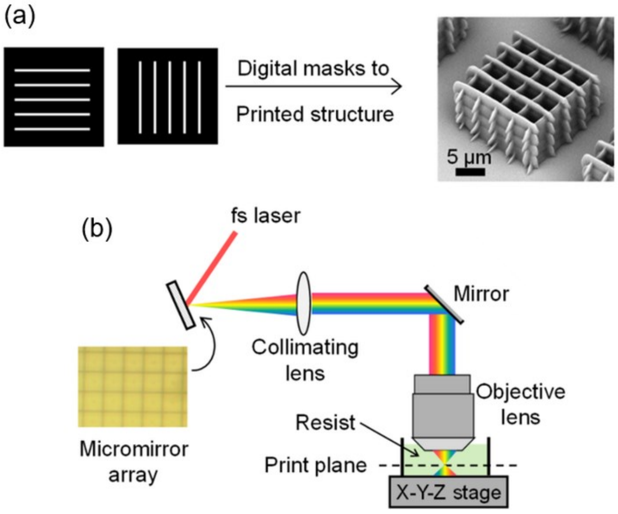
(a)
Digital masks to
Printed structure
5 µm
(b)
fs laser
Mirror
Collimating lens
Objective lens
Resist
Micromirror array
Print plane
X-Y-Z stage

Figure 2:

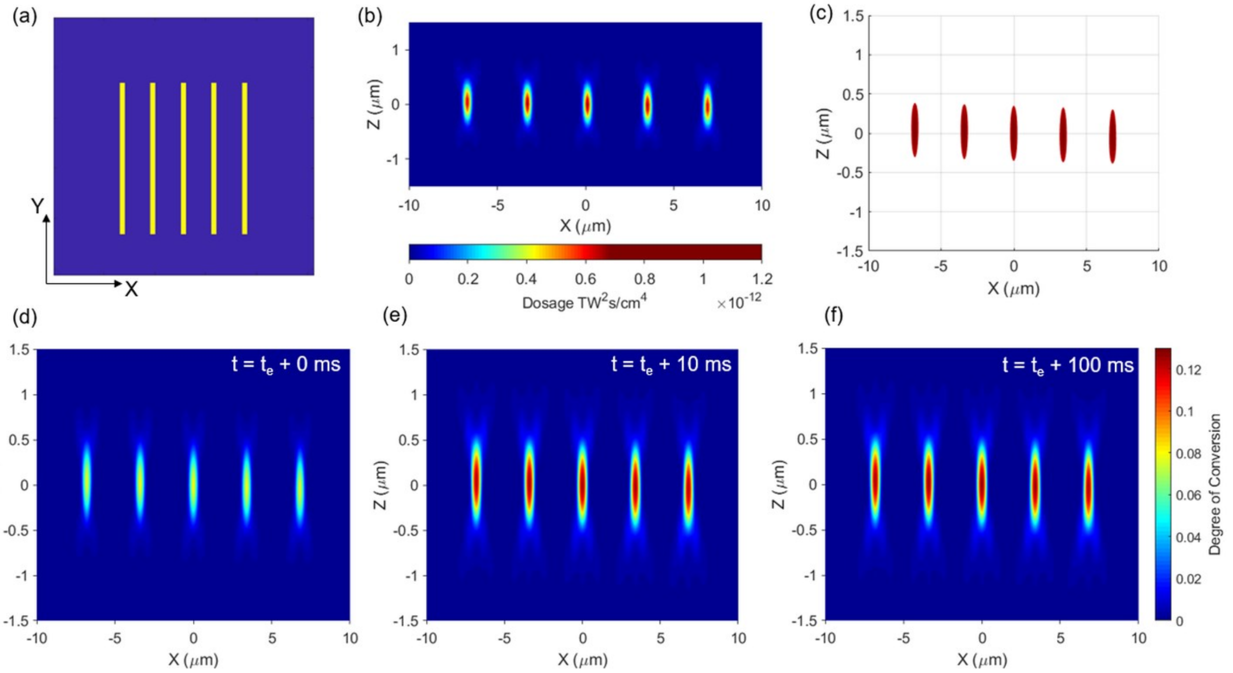
(a)
Y
X
(b)
Z (μm)
X (μm)
Dosage TW^{2}s/cm^4
×10^{-12}
0
0.2
0.4
0.6
0.8
1
1.2
(c)
Z (μm)
X (μm)
(d)
t = t$_e$ + 0 ms
(e)
t = t$_e$ + 10 ms
(f)
t = t$_e$ + 100 ms
Z (μm)
X (μm)
Degree of Conversion
0
0.02
0.04
0.06
0.08
0.1
0.12
-10
-5
0
5
10
-1.5
-1
-0.5
0.5
1
1.5

Figure 3:

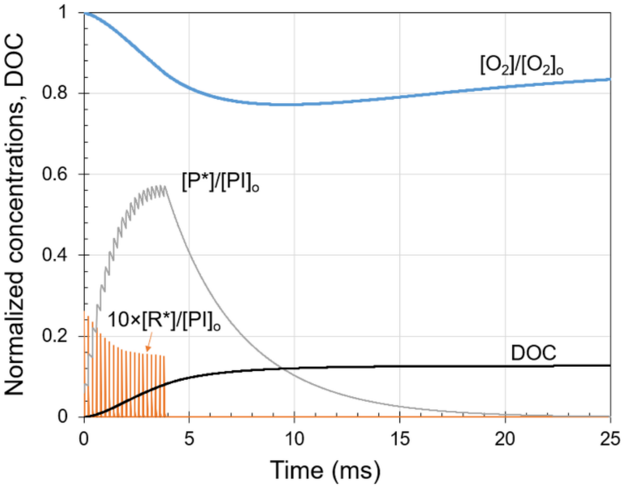
[O$_2$]/[O$_2$]$_o$
[P*]/[PI]$_o$
10×[R*]/[PI]$_o$
DOC
Normalized concentrations, DOC
Time (ms)
1
0.8
0.6
0.4
0.2
0
0
5
10
15
20
25

Figure 4:

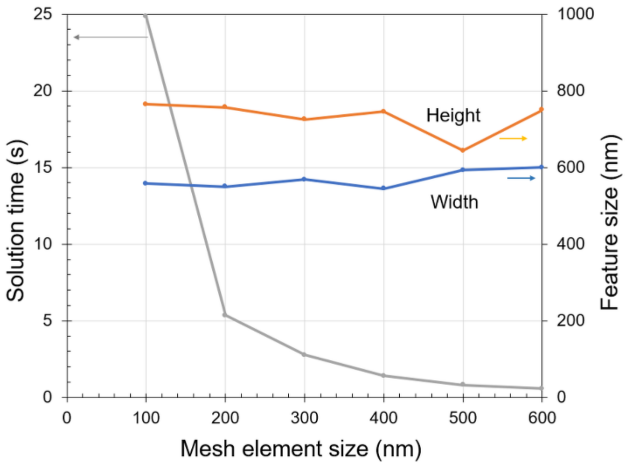
25
20
15
10
5
0
Solution time (s)
1000
800
600
400
200
0
Feature size (nm)
0
100
200
300
400
500
600
Mesh element size (nm)
Height
Width

Figure 5:

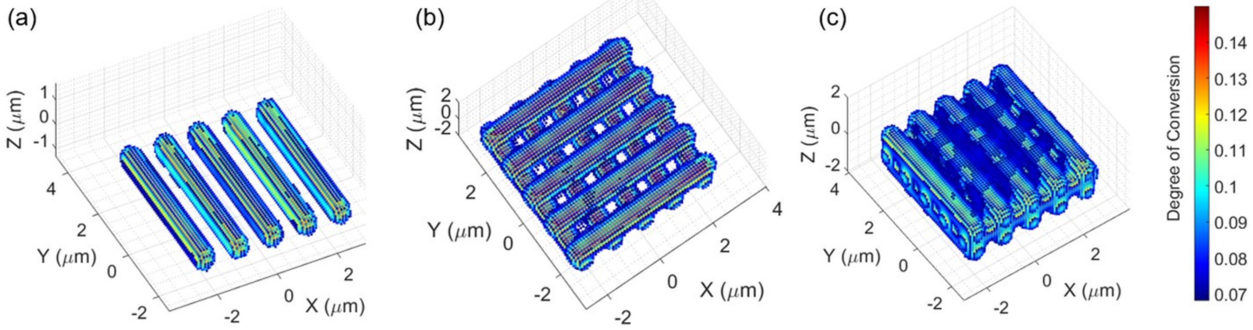
(a)
(b)
(c)
Z (μm)
Y (μm)
X (μm)
Degree of Conversion
0.07
0.08
0.09
0.1
0.11
0.12
0.13
0.14

Figure 6:

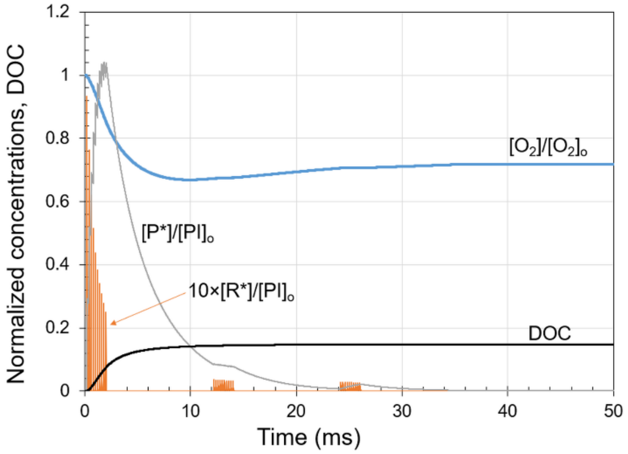
1.2
1
0.8
0.6
0.4
0.2
0
Normalized concentrations, DOC
0
10
20
30
40
50
Time (ms)
[O$_2$]/[O$_2$]$_o$
[P*]/[PI]$_o$
10×[R*]/[PI]$_o$
DOC

Figure 7 :

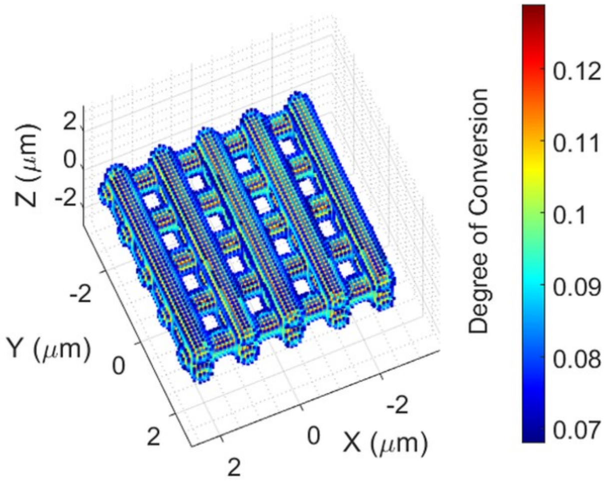
Z (μm)
2
0
-2
Y (μm)
-2
0
2
X (μm)
2
0
-2
Degree of Conversion
0.12
0.11
0.1
0.09
0.08
0.07

Figure 8:

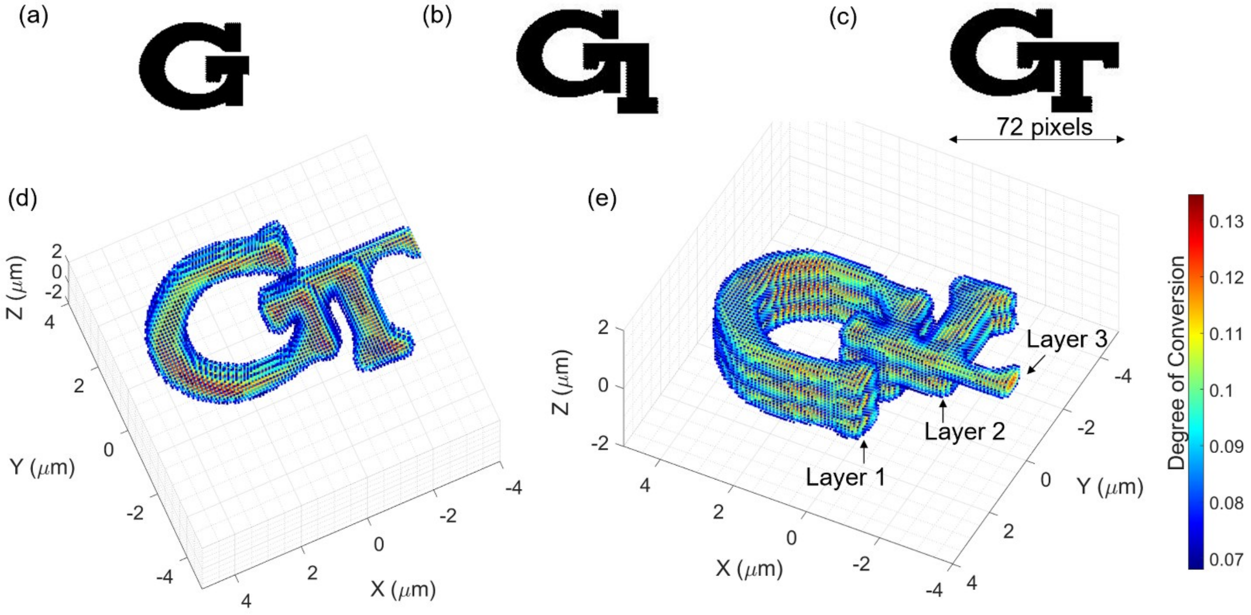
(a)
(b)
(c)
72 pixels
(d)
Z (μm)
2
0
-2
4
2
0
-2
-4
Y (μm)
4
2
0
-2
-4
X (μm)
(e)
Layer 3
Layer 2
Layer 1
Z (μm)
2
0
-2
4
2
0
-2
-4
X (μm)
-4
-2
0
2
4
Y (μm)
Degree of Conversion
0.13
0.12
0.11
0.1
0.09
0.08
0.07

Figure A1 :

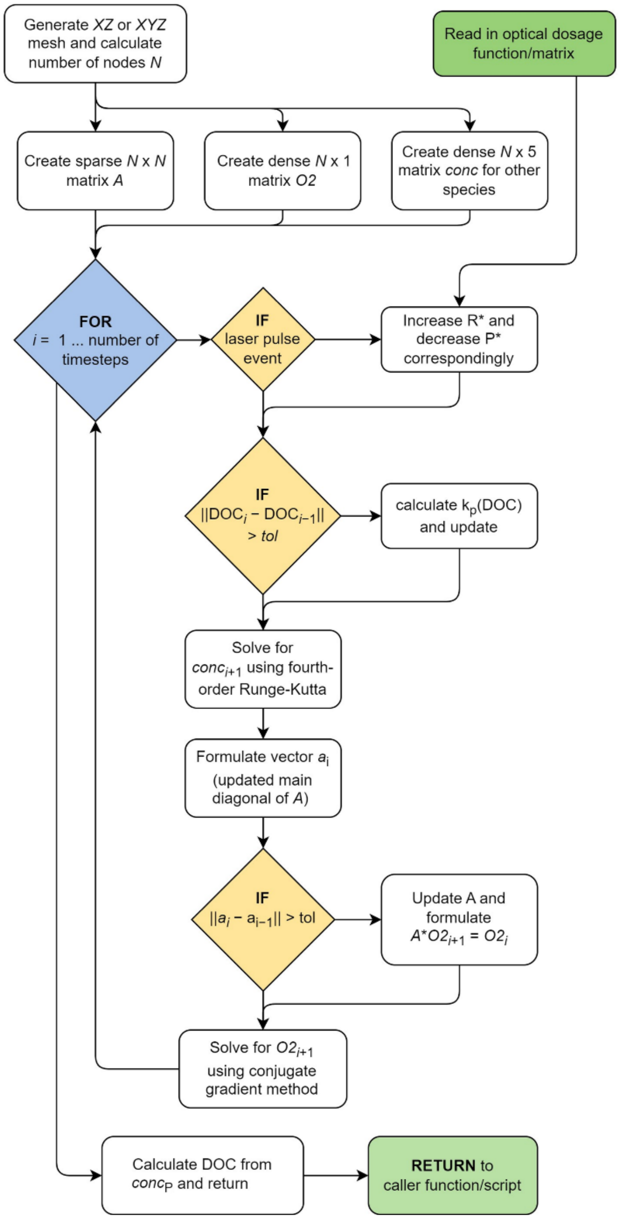

Generate XZ or XYZ mesh and calculate number of nodes N
Read in optical dosage function/matrix
Create sparse N x N matrix A
Create dense N x 1 matrix O2
Create dense N x 5 matrix conc for other species
FOR i = 1 ... number of timesteps
IF laser pulse event
Increase R* and decrease P* correspondingly
IF ||DOC_i − DOC_i−1|| > tol
calculate k_p(DOC) and update
Solve for conc_i+1 using fourth-order Runge-Kutta
Formulate vector a_i (updated main diagonal of A)
IF ||a_i − a_i−1|| > tol
Update A and formulate A*O2_i+1 = O2_i
Solve for O2_i+1 using conjugate gradient method
Calculate DOC from conc_P and return
RETURN to caller function/script

Table Captions List

Table 1: Parameters for the reaction-diffusion model

Table 2: Initial conditions for OS-FDM and FE models

Table 3: Performance of OS-FDM versus FE models

Table 1

Parameter	Value	Source
$\sigma^{(2)}$	133×10^{-50} cm^4s/photon-molecule	Estimate from Rumi et al. (Fig. 5, compound 8 of reference [38])
h	6.626×10^{-34} m^2 kg / s	Fundamental constant
k_p	4.3×10^4 dm^3 $mol^{-1}s^{-1}$	Mueller et al. [19]
k_q	2.3×10^6 dm^3 $mol^{-1}s^{-1}$	Mueller et al. [19]
k_t	5.9×10^4 dm^3 $mol^{-1}s^{-1}$	Calibrated using empirical data [37]
	0.0061	Calibrated using empirical data [37]
DOC_{th}	0.068	Measured [37]
D_{O2}	1.2×10^{-12} m^2 s^{-1}	Estimated using Stokes-Einstein equation
v	375 THz	Printer laser

Table 2

Parameter	Initial value	Source
$[O_2]$	6×10^{-3} mol dm^{-3}	Mueller et al. [19]
[PI]	1.65×10^{-3} mol dm^{-3}	Resist composition, PI at 0.1% by weight
[P]	4.0 mol dm^{-3}	Material datasheet [37]
$[R^*]$, $[P^*]$	0 mol dm^{-3}	No light exposure at $t = 0$
$[R^x]$, $[P^x]$	0 mol dm^{-3}	No reaction products at $t = 0$

Table 3

Model	**Discretization parameters**	**Time to solve (s)**	**Mean width (nm)**	**Mean height (nm)**	**Width error (%)**	**Height error (%)**
FE	Tolerance = 10^{-10}	8207	531	741	0	0
FE	Tolerance = 10^{-8}	3403	531	744	0.3	0.4
FE	Tolerance = 10^{-4}	249	585	822	10.5	10.9
OS-FDM	Node spacing = 100 nm	25	508	703	4.6	5.2
OS-FDM	Node spacing = 200 nm	5	495	693	7.0	6.5